

## Article

# Influence of Processing Temperature and Strain Rate on the Microstructure and Mechanical Properties of Magnesium Alloys Processed by Single-Pass Differential Speed Rolling

Christopher Hale, Zhigang Xu \*, Svitlana Fialkova, Jessica Rawles and Jagannathan Sankar

Department of Mechanical Engineering, North Carolina A&T State University, Greensboro, NC 27411, USA; clhale@aggies.ncat.edu (C.H.); sfialkov@ncat.edu (S.F.); jrlawles@aggies.ncat.edu (J.R.); sankar@ncat.edu (J.S.)

\* Correspondence: zhigang@ncat.edu

**Abstract:** Magnesium-based alloys show significant promise for widespread applications owing to their lightweight nature and improved mechanical properties achieved through grain refinement via hot rolling. This investigation focuses on Mg-xAl-yCa-zMn (AXM alloys), pre-heated to temperatures of 350, 400, and 450 °C and processed via both single-pass differential speed rolling (DSR) and conventional rolling (CR). The key findings reveal the interplay between processing temperature, strain rate during single-pass rolling, and an innovative approach for incorporating varying amounts of Ca, influencing grain size, quantity of dynamic recrystallization (DRX) grains, and overall mechanical properties, including strength and ductility. A noteworthy observation is the positive correlation between an increase in the total reduction during hot rolling and a higher fraction of DRXed grains. This leads to a significant reduction in average grain size, diminishing from  $60.3 \pm 54.3 \mu\text{m}$  to  $19.5 \pm 14.2 \mu\text{m}$  at 40%, nearly a third the size of T4 grains (the initial homogenized microstructure of the AXM alloys). The resultant material strength experiences a doubling from an average of  $125 \pm 10.2 \text{ MPa}$  (T4) to  $260 \pm 25.8 \text{ MPa}$  (DSR rolled at 40%) for the AXM alloys with potential improvement in the ductility depending on rolling speed conditions. This study also aims to analyze the combination of rolling temperature, rolling speed, thickness reduction, speed difference and Ca content implemented across a wide range of temperatures and strain rates to provide a holistic approach to the processing parameters affecting the microstructure and mechanical properties of AXM alloys. Furthermore, this study provides a deeper understanding of DRX mechanisms, including continuous DRX (CDRX), discontinuous DRX (DDRX), and twinning induced DRX (TDRX), while each of these mechanisms plays a distinct role in the overall enhancement of formability and performance of magnesium alloys.

**Keywords:** magnesium alloys; single-pass rolling; mechanical properties; tensile testing; differential speed rolling



**Citation:** Hale, C.; Xu, Z.; Fialkova, S.; Rawles, J.; Sankar, J. Influence of Processing Temperature and Strain Rate on the Microstructure and Mechanical Properties of Magnesium Alloys Processed by Single-Pass Differential Speed Rolling. *Crystals* **2024**, *14*, 262. <https://doi.org/10.3390/cryst14030262>

Academic Editor: Subbarayan Sivasankaran

Received: 17 January 2024

Revised: 29 February 2024

Accepted: 2 March 2024

Published: 6 March 2024



**Copyright:** © 2024 by the authors. Licensee MDPI, Basel, Switzerland. This article is an open access article distributed under the terms and conditions of the Creative Commons Attribution (CC BY) license (<https://creativecommons.org/licenses/by/4.0/>).

## 1. Introduction

Magnesium-based alloys are recognized as some of the lightest structural metallic materials, making them promising for applications in industries such as automotive and aerospace [1–3]. However, a notable drawback is their lower strength and ductility, presenting challenges for practical use in manufacturing magnesium-based products [4–6]. While the addition of rare-earth (RE) elements has been shown to enhance the mechanical properties of these alloys, the high cost associated with RE elements limits their widespread use in large-scale industrial applications [7–9]. Consequently, there is a growing emphasis on the development of novel RE-free magnesium alloys that can offer optimal mechanical properties.

Among the widely used magnesium-aluminum (Mg-Al) based alloys are AZ31, AZ91, and AXM60, chosen for their excellent castability, improved strength, and high

formability [10–12]. Despite these advantages, the strength of Mg-Al-based alloy sheets remains relatively low, typically below 300 MPa [13,14]. This limitation underscores the need for ongoing research and development efforts aimed at further enhancing the mechanical properties of Mg-Al alloys. Other systems include the Mg-7Li-1Zn alloy that have desirable formability due to the high slip system in ambient temperature [15].

One avenue for improvement involves grain refinement, a process known to effectively enhance the strength and ductility of magnesium alloys. This is achieved through severe plastic deformation (SPD) methods such as equal channel angular pressing (ECAP) and differential speed rolling (DSR) [16–18]. However, in many industrial settings, the implementation of ECAP and DSR processes can be prohibitively expensive and challenging to scale up for large-scale production [19,20].

An alternative approach involves the use of low-alloyed RE-free Mg alloys, leveraging their excellent hot-working performance and cost-effectiveness. While much attention has been given to traditional Mg-Al-Zn alloy sheets, there is a notable gap in research focusing on novel Ca-containing Mg-Al-based alloys. The addition of calcium (Ca) is considered a more affordable and lightweight alloying option capable of improving the mechanical properties of Mg alloys. Studies, such as those by Wang et al. [13] and Zubair et al. [21], have demonstrated the positive impact of adding Ca to Mg-Al alloys, resulting in increased ultimate tensile strength (UTS) and yield strength (YS). However, a trade-off with ductility is often observed.

The Mg-Al-Ca system is regarded as especially interesting to produce high strength components in industrial settings. The system uses relatively cheap and abundant alloying elements and can offer a multitude of processing possibilities. Aluminum is the most important alloying element for Mg, both for casting and wrought alloys, as it increases the castability and mechanical strength and enables the ability of work hardening [22,23]. Calcium is used for grain refinement of the cast material [24,25]. Mn is often added to these alloys as it binds Fe, thereby reducing the corrosion tendency [26]. Moreover, Al-Mn dispersoids inhibit grain growth during processing and solution heat treatment by Zener drag [5,27]. Overall, the Mg-Al-Ca-Mn alloy has been shown to exhibit high strength due to the broad range of Ca and Al in the system [28].

Investigations into Mg-Al-Ca-Mn (AXM) alloys have revealed dynamic microstructure evolution and mechanical property enhancements during hot rolling. The formation of extension twins, double twins, and continuous dynamic recrystallized grains has been observed, with the process influenced by factors such as rolling temperature, rolling speed, reduction rate, speed difference, and Ca content [29].

The study encompasses a thorough evaluation of several critical factors to understand their influence on the microstructure and mechanical properties of AXM alloys. Each factor, including rolling temperature, rolling speed, thickness reduction, speed difference, and calcium content, plays a crucial role in shaping the alloy's characteristics.

Rolling temperature, a pivotal processing parameter, affects the deformation mechanisms in Mg alloys, such as non-basal slip and dynamic recrystallization (DRX) [30]. Research with Mg-Zn based alloys has shown that lower temperatures have resulted in higher strength but slightly lower ductility, whereas higher temperatures offer better ductility with slightly lower strength. More intermediate temperatures have shown optimization in the balance between strength and ductility [31,32].

Rolling speed is another significant parameter that influences deformation mechanisms, with twinning dominating at lower speeds and dynamic recrystallization constrained to shear bands. Higher speeds, on the other hand, extend dynamic recrystallization, leading to a more homogenous microstructure. This research has shown tensile ductility gradually improves with increasing rolling speed, attributed to enhanced dynamic recrystallization [33]. Thickness reduction is another key parameter impacting the homogeneity and fine-grained structure of Mg alloys and research has shown that a larger thickness reduction results in more homogenous and fine-grained structures compared to smaller reductions [34]. The speed difference, or the difference in speed between the top



The evaluation of AXM samples adheres to the design principle, focusing on the Ca/Al ratio in the as-cast, T4, and rolled conditions. To improve the strength and ductility of AXM wrought alloys, it is critical to modify the type and amount of eutectic phases by controlling the alloy composition. Studies have shown it is possible to develop high-strength Mg-Al-Ca-Mn alloys with higher Ca/Al ratios but with sacrifice to ductility. To achieve a balance in high strength and high ductility, a lower Ca/Al ratio and lean composition is preferred as seen in Table 1 which provides a comprehensive overview of the AXM alloys' compositions and a range of Ca/Al ratios.

**Table 1.** Composition of AXM alloys with varying amounts of Ca.

Alloys	Wt% Mg	Wt% Al	Wt% Ca	Wt% Mn	Ca/Al wt
AXM201504	97.45	2.0	0.15	0.4	0.075
AXM20504	97.1	2.0	0.5	0.4	0.25
AXM21004	96.6	2.0	1.0	0.4	0.5
AXM21504	96.1	2.0	1.5	0.4	0.75

The Mg-xAl-yCa-zMn alloy used in this study was fabricated by melting high-purity Mg (99.97%, US Magnesium LLC, Salt Lake City, UT, USA) and Al (99.9999%, Alfa Aesar, Haverhill, MA, USA) as well as master alloys Mg-20Ca and Mg-5Mn at 730 °C and casting the melt into a preheated permanent steel mold in an argon-filled glove box, as carried out for other Mg-based alloys in previous studies [38]. Specifically, pure Mg was melted at 730 °C followed by the addition of pure Al, Mg-Ca, and Mg-Mn master alloys and a holding for 10 min, and a mechanical stirring for 15 min to homogenize the melt. This, in turn, was followed by extra dwelling at 690 °C for 1 h. Before casting, the temperature of the melt was raised to 730 °C. The melt was cast through a magnesia foam filter (15 pores per inch) into the steel book mold preheated to 250 °C. Plates with dimensions of 100 mm (length) × 20 mm (width) × 4 mm (thickness) were cut from the as-cast ingots as starting materials. To improve the uniformity of the microstructure, the as-cast plates were homogenized and then quenched in water [38].

The simulated phase diagram was used to guide the determination of solution heat treatment temperatures for all compositions. To prevent the presence of a liquid phase, solution treatment temperatures of 470 °C and 500 °C were selected for evaluation in the case of AXM20504. Both the temperatures 470 and 500 °C were examined over a period of up to 40 h, as illustrated in the heat treatment diagram in Figure 2. At the end of different heat times, specimens were water-quenched and polished. They were then etched and observed using an optical microscope. The area fraction of the residual second phases was analyzed with Image Pro Plus to evaluate the completeness of the heat treatment. Depending on the outcomes for AXM20504, one condition for solution heat treatment was selected and subsequently applied to the remaining alloy compositions. The heat treatment of 500 °C for 30 h was chosen for the T4 condition based on minimizing second phase area fraction and minimal grain growth. This criterion was then applied to three alloys based on location in the phase diagram (AXM20504, AXM21004, and AXM21504), while a temperature of 520 °C for 30 h was implemented for AXM201504 due to the extreme wt% Ca as seen on the phase diagram. These conditions minimized both the area fraction of the second phase and minimized grain growth for the T4 condition for each alloy.

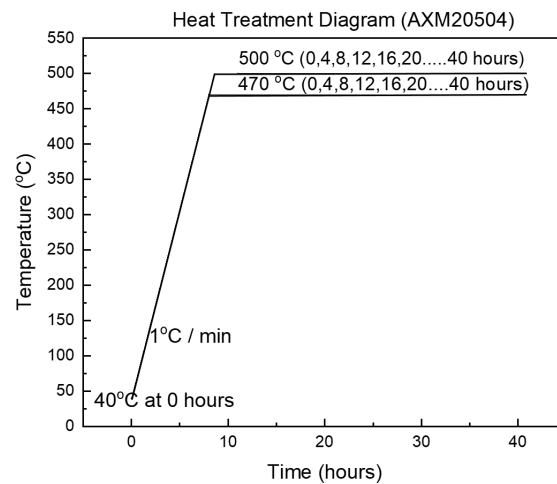


**Figure 2.** Solution treatment diagram of Mg-xAl-yCa-zMn (AXM20504) showing the time versus temperature for AXM20504.

### 2.2. Design of the Rolling Process

After heat treatment, the ingots for each composition underwent cutting into plates with dimensions of 20 mm width, 110 mm length, and 4 mm thickness, specifically prepared for differential speed rolling (DSR) and conventional rolling (CR). Prior to rolling, the AXM samples designated for DSR and CR were subjected to pre-heating at temperatures of 350, 400, and 450 °C, all temperatures determined through analysis of the phase diagram.

The diameters of the upper and lower rolls are identical (100 mm) and the speed ratio between the upper and the lower rolls is adjustable. The rolls were maintained at a constant temperature of 300 °C by resistance heating elements that are embedded inside the rolls. No lubrication was applied during rolling. The pre-heated plates were fed between the rolls consistently for microstructural and mechanical property studies [38].

Different rolling speeds were employed for DSR, denoted as DSR 4–2, DSR 2–1, DSR 1.2–0.6, DSR 0.8–0.2, DSR 0.6–0.2, and DSR 0.4–0.2. Similarly, various rolling speeds were employed for CR, including CR 3–3, CR 1.5–1.5, CR 0.9–0.9, and CR 0.3–0.3. These rolling speeds were chosen to encompass a wide range of strain rates considered for the comparison of DSR and CR. In these rolling speed conditions, the first digit represents the speed of the upper roll, and the second digit represents the speed of the lower roll in m/min with a custom-made rolling mill (International Rolling Mills in Rhode Island, USA). Table 2 below outlines AXM-alloy thickness reduction rates and thicknesses after rolling.

**Table 2.** Reduction rate and final thickness of AXM alloys for DSR and CR.

Sample Set	Reduction Rate (%)	Final Thickness (mm)
1	10	3.56 ± 0.05
2	20	3.18 ± 0.09
3	30	2.78 ± 0.03
4	40	2.48 ± 0.06

### 2.3. Microstructural Characterization

Microstructural features were characterized on the ND plane using optical microscopy (OM, Zeiss, AxioCam MRC5, Oberkochen, Baden-Württemberg, Germany), scanning electron microscopy (SEM, Hitachi, SU8000, Chiyoda City, Tokyo, Japan), and energy dispersive X-ray spectroscopy (EDS). The T4 heat-treated alloys were observed with OM/SEM to identify suitable conditions for solution-treating the materials. Specimens for microstructural analysis were carefully sectioned to the normal surface (ND).

The AXM alloys (201504, 20504, 21004, and 21504) were prepared for OM metallography using standard mechanical grinding with SiC papers and final polishing using 0.05  $\mu\text{m}$   $\text{Al}_2\text{O}_3$  suspension to the middle of the sample thickness. Subsequently, the samples were etched with a mixture of 10% nitric acid and picric acid to highlight grain boundaries for optical microscopy. Following the etching process, the samples were cleaned with isopropanol and dried to ensure readiness for optical microscopy examination. Grain size analysis for the optical microscopy (OM) samples was conducted using the mean linear intercept method.

Following the evaluation of microstructural features using optical microscopy (OM) for the four compositions, the specimens were subjected to cleaning and polishing for scanning electron microscopy (SEM). Images were captured at various magnifications, including 50 $\times$ , 200 $\times$ , 500 $\times$ , and 1000 $\times$ , to closely examine microstructural features such as grain size and second-phase precipitates.

The crystallographic phase content for the as-cast, T4 treated, and DSR processed AXM20504 alloys were evaluated by X-ray diffractometry. The X-ray diffraction analysis was performed using Bruker D8 Advance diffractometer (Bruker Corp., Billerica, MA, USA) using  $\text{CuK}\alpha$  radiation at 40 mA and 40 kV. The data collected in the  $2\theta$  range of 20–80 $^\circ$ , at a step of 0.02 $^\circ$  and a step time of 0.5–1 s were used. Phase identification was accomplished using a search-match “EVA” software (version 5.2) utilizing the JCP database.

Samples for EBSD were first polished in the same manner as those for OM, followed by further polishing with an ion mill (Fischione, Model 1061 SEM Mill, Export, PA, USA) for 4 h with the parameters of 3 kV and 3 $^\circ$  tilt. EBSD allowed for the generation of inverse pole figure (IPF) maps and pole figures, facilitating the examination of the quantity and grain size of dynamically recrystallized (DRX) grains. The EBSD analysis utilized acquisition parameters of 15 kV and 20  $\mu\text{A}$ , employing a Symmetry EBSD detector from Oxford Instruments, Abingdon, Oxfordshire, UK), attached to an SU8000 cold cathode field emission SEM from Hitachi High-Tech (Tokyo, Japan). The Aztec and Aztec Crystal software Version 2.2.302 (2021) played a pivotal role in conducting various measurements and analyses, including DRX grain measurements, area fraction measurements, misorientation angles, pole figures, tilt angles, and low/high grain boundary angles. The integration of EBSD and associated software contributed to a comprehensive understanding of the microstructural characteristics, offering insights into the amount and size of DRXed grains and the orientation of the grains with pole intensity determination. The samples for microstructural evaluation were cut and polished to the middle for microstructural analysis with OM, SEM, and EBSD analysis of the normal direction (ND).

#### 2.4. Mechanical Testing

Subsequently, three tensile testing specimens were meticulously prepared according to ASTM E8/ASTM E8M using wire-EDM for each rolling condition and from the T4 heat-treated ingots of the AXM alloys. The cutting direction of the tensile specimens is parallel to the rolling direction. Dimensions at the gauge section were 15 mm in length, 3.0 mm in width, and 3.0 mm in thickness.

The samples underwent tensile testing using the Instron Model 5566 machine (Instron, Norwood, MA, USA), where data was systematically collected at estimated strain rate of  $1.3 \times 10^{-3} \text{ s}^{-1}$ . The key parameters obtained included the yield strength, ultimate tensile strength, and percent elongation for each of the tensile specimens. These measurements contribute to a comprehensive understanding of the mechanical properties of the materials under different rolling conditions and compositions.

### 3. Results

#### 3.1. Microstructure of AXM Alloys

Figure 3 shows the optical micrographs illustrating the microstructures of the AXM alloys in both the as-cast and T4 conditions, showing solution-treated material. The as-cast alloys are presented in panels (a) through (d) for AXM201504, AXM20504, AXM21004, and

AXM21504, respectively. Notably, the as-cast condition for each composition (Figure 3a–d) exhibits a higher presence of the second phase compared to the T4 condition (Figure 3e–h), indicating a more homogenized microstructure following heat treatment.

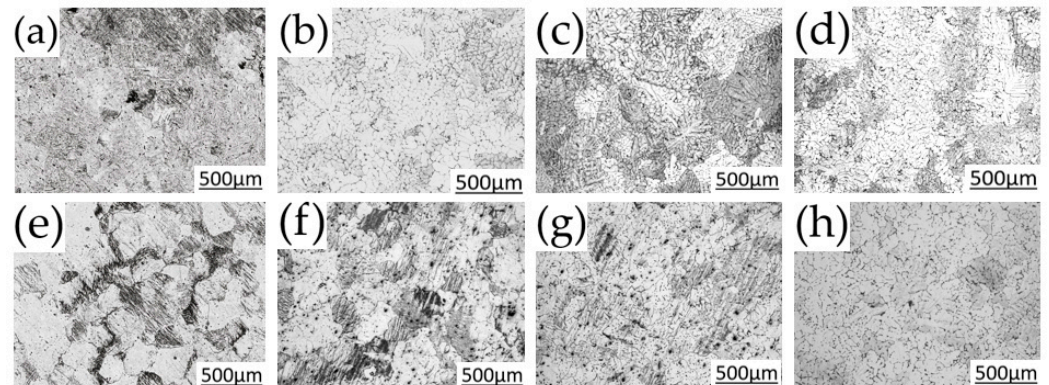


**Figure 3.** Optical micrographs on the ND plane of (a–d) in as-cast condition and (e–h) in T4 condition for each alloy composition (AXM201504, AXM20504, AXM21004, and AXM21504, respectively).

In Figure 4, the XRD spectra of alloy AXM20504 in as-cast, T4, and processed with DSR at 40% reduction at 400 °C are depicted. The spectra for the as-cast reveal the presence of intermetallic secondary phases as shown in black. After solution heat treatment, the peak exhibited a more uniform microstructure, as represented in blue exhibiting only very small trace amounts of phase, totaling less than 3%. Finally, the DSR rolled condition at 40% reduction and 400 °C, shown in red, displays 6% identifiable phases, with 3% attributed to AlMn and another 3% to Al<sub>3</sub>Mg<sub>2</sub>. This observation is crucial as it confirms the presence of the second phase in the rolled material, corroborating findings from both energy dispersive spectroscopy (EDS) and electron backscatter diffraction (EBSD). The second phase is significant for strengthening the alloy but can also hinder dislocation movement, potentially reducing the material's ductility.

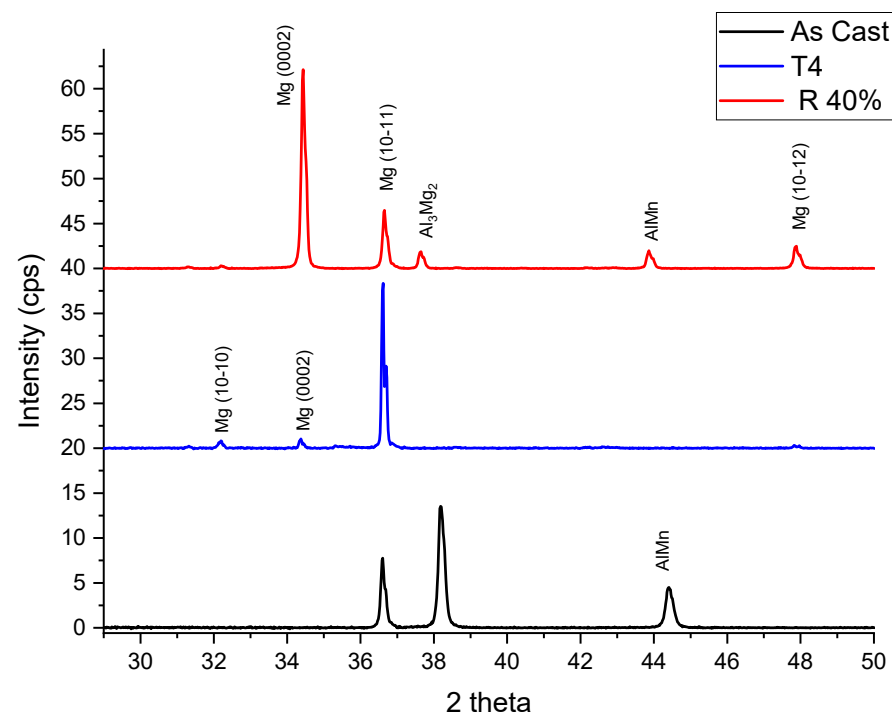


**Figure 4.** XRD showing as-cast, T4 state and 40% DSR (400 °C) of the AXM20504.

Figure 5 illustrates AXM20504 after DSR processing with second-phase precipitates mostly arranged around the grains, as indicated by the black arrow. The EDS composition is also provided to the right, supporting the identification of the second phase. Similar alloys have been reported to have microstructures consisting of fragmented Ca-containing phases and Al-Mn phase particles. These robust intermetallic phases have been shown to enhance dynamic recrystallization during thermomechanical processes. Furthermore, these intermetallic particles play a crucial role in impeding the motion of grain boundary slip, thereby improving the material's strength and creep resistance at elevated temperatures [10].

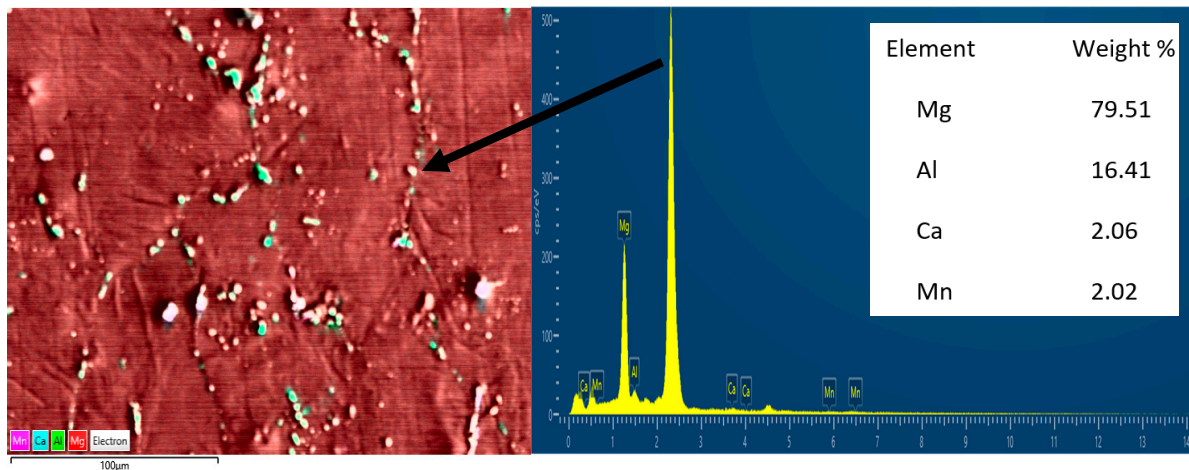


**Figure 5.** EDS showing the second phase around grains of AXM20504 on the ND plane (DSR 40% and 350 °C) consisting of  $\text{Al}_3\text{Mg}_2$  and  $\text{AlMn}$ .

In Figure 6a, the EBSD inverse pole figure (IPF) map demonstrates the T4 condition for the alloy AXM20504, while Figure 6b showcases the IPF maps for the same alloy rolled with speeds of 4:2 m/min at temperatures of 350, 400, and 450 °C for reductions ranging from 10 to 40%. The IPF map for the solution-treated AXM20504 indicates that the original grain size before rolling was  $60.3 \pm 54.3 \mu\text{m}$ , as well as the random orientations of the grains. At a 40% reduction, the average grain size reduced significantly to approximately  $19.5 \pm 14.2 \mu\text{m}$ . These maps provide a representation of the changes in grain structure resulting from the rolling process, offering insights into the grain refinement achieved at different reduction levels and temperatures.

In Figure 7, the inverse pole figure (IPF) maps for the ND plane of AXM20504 are presented for various rolling speeds using both differential speed rolling (DSR) and conventional rolling (CR) at 40% reduction and 400 °C for comparison. The IPF maps are shown at  $50\times$  magnification (top) and  $500\times$  magnification (bottom). At  $50\times$  magnification, the grain refinement is evident for the different rolling speeds, displaying a 4:1 ratio on the left, followed by ratios of 3:1 and 2:1. The DSR grain refinement resulted in an average grain size ranging from 18 to 22  $\mu\text{m}$ , a notable reduction from 60.3  $\mu\text{m}$  at the T4 condition. All sample conditions exhibited grain refinement with successive reduction which indicated an increase in strain rate. The IPF maps provide a demonstration of the impact of rolling speed on grain structure, emphasizing the effectiveness of DSR in achieving grain refinement across various conditions. The difference in average DRX grain size for the various speed ratios was within a few microns as can be seen in Figure 7 which compares the DSR and CR rolling of the AXM20504.

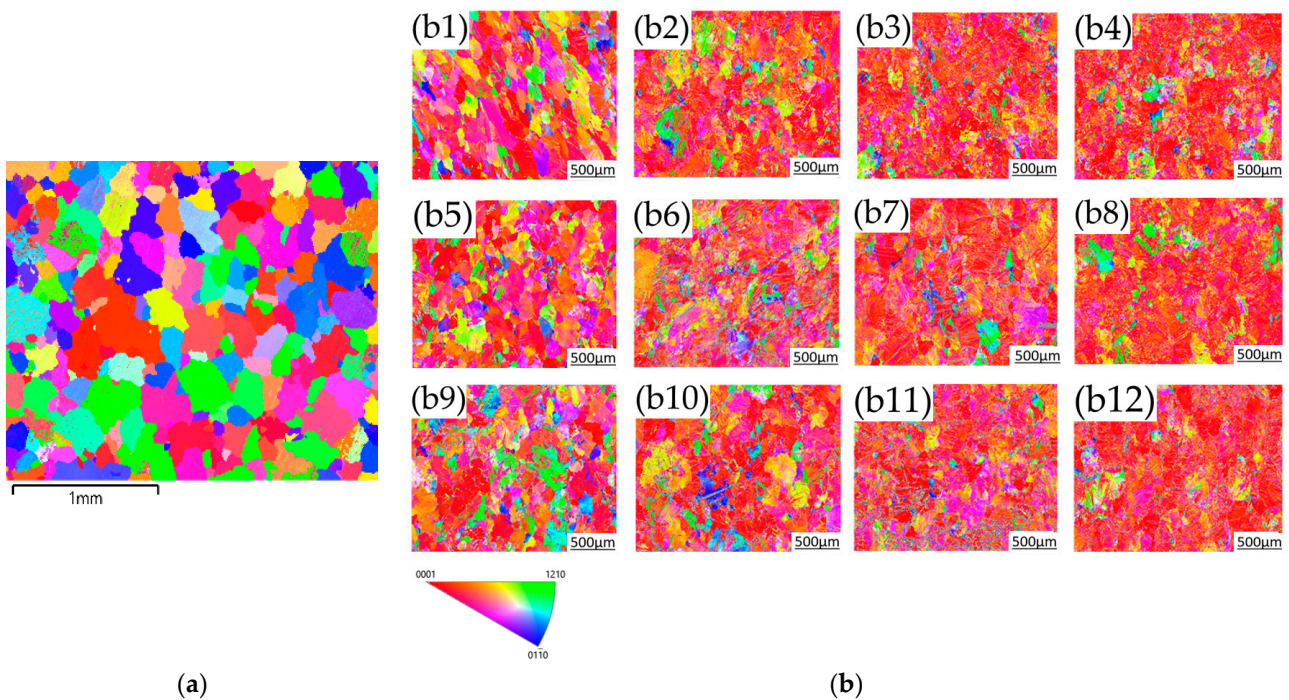


**Figure 6.** (a). Inverse pole figure (IPF) map of T4 on the ND plane for AXM20504 showing initial grain size. (b). Inverse pole figure (IPF) maps on the ND plane for the AXM20504 plates rolled with speeds of 4:2 m/min and temperatures 350, 400, and 450 °C and rolling thickness reductions from 10 to 40%. Grain refinement is seen with successive rolling reduction at (b1) 10%, (b2) 20%, (b3) 30%, and (b4) 40% at 350 °C. Likewise, it applies for (b5) 10%, (b6) 20%, (b7) 30%, and (b8) 40% at 400 °C as well as (b9) 10%, (b10) 20%, (b11) 30%, and (b12) 40% at 450 °C.

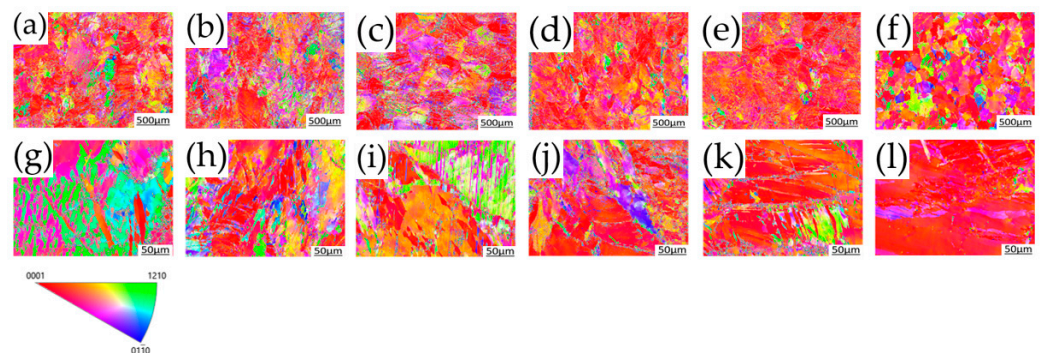


**Figure 7.** Inverse Pole Figure (IPF) maps on the ND plane for AXM20504 alloy for various DSR rolling speed ratios at 40% and 400 °C. Ratios include (a) 0.8–0.2, (b) 0.6–0.2, (c) 0.4–0.2, (d) 1.2–0.6, (e) 2–1, and (f) 4–2 m/min which are scanned all at 50 $\times$ . Likewise, (g–l) shows the respective rolling speeds at 500 $\times$ .

In Figure 8, the conventional rolling (CR) processed AXM20504 is depicted, illustrating finer grains at both 50 $\times$  magnification (top) and 500 $\times$  magnification (bottom). The CR-processed AXM20504 exhibits a comparable level of grain refinement, with a similar average DRX grain size as observed in the DSR-processed material, as shown in Figure 9. This suggests that both processing methods, DSR and CR, contribute to effective grain refinement in AXM20504, and the resulting microstructures are comparable in terms of grain size reduction. The visual representation provided by the IPF maps aids in the understanding of the microstructural changes induced by different rolling processes.

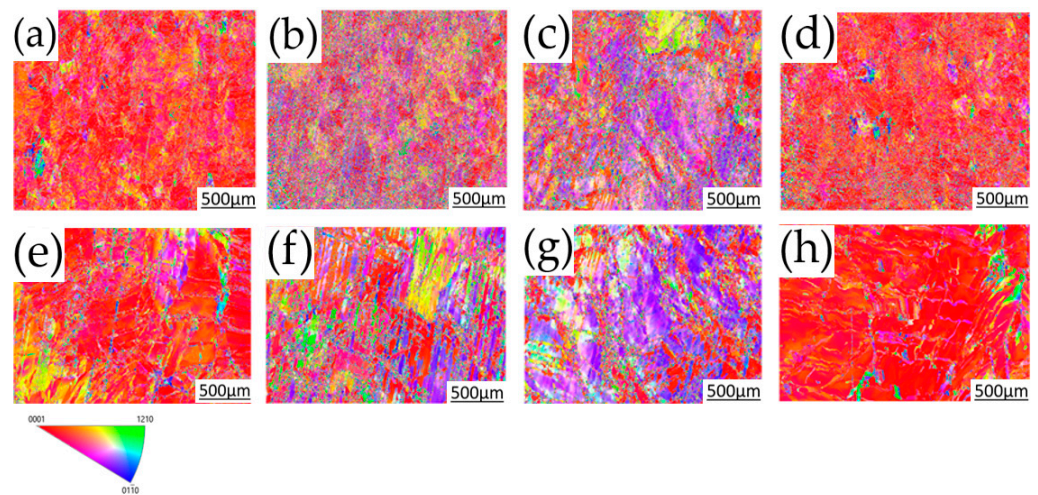


**Figure 8.** EBSD IPF maps for AXM20504 for different CR rolling speeds at thickness reduction and temperature of 40% and 400 °C, respectively. They include (a) 0.3–0.3, (b) 0.9–0.9, (c) 1.5–1.5, and (d) 3.0–3.0 m/min scanned at 50 $\times$ . Likewise, (e–h) are for the same speeds as above but at 500 $\times$ .

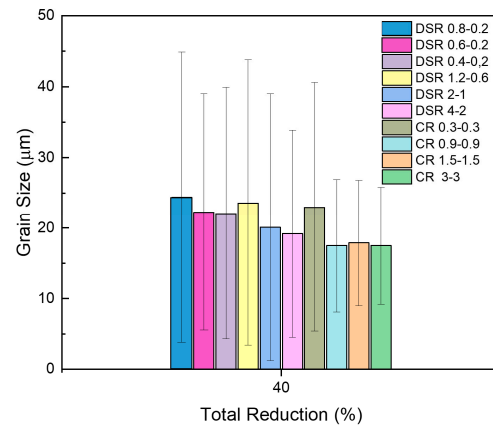


**Figure 9.** The grain size of the AXM20504 shows the influence of rolling speed, each at 40% reduction and 400 °C. Rolling speed ratios include DSR 4:1 (0.8–0.2), DSR 3:1 (0.6–0.2), DSR 2:1 (0.4–0.2; 1.2–0.6; 2–1; 4–2) and CR 1:1 (0.3–0.3; 0.9–0.9; 1.5–1.5; 3.0–3.0).

Figure 9 illustrates the impact of the rolling speed ratio on grain size refinement, demonstrating a narrow window in the final grain size with an average size ranging from 18 to 22  $\mu\text{m}$ . This range is consistent between both differential speed rolling (DSR) and conventional rolling (CR), indicating the similarity in grain size. Unlike some magnesium alloys such as AZ31, where increasing the rolling speed ratio results in more apparent grain refinement and higher strength along with higher ductility [39], the results for AXM alloys in Figure 9 suggest that higher speed ratios for DSR did not significantly differ in final grain sizes compared to their CR counterparts. The findings provide insights into the specific behavior of AXM alloys in response to different rolling speed ratios, emphasizing the importance of understanding alloy-specific characteristics in the optimization of rolling processes.

Figure 10 provides insight into the distribution of low-angle/high-angle grain boundaries for alloy AXM20504. As the reduction increases from 10% to 20%, 30%, and 40% in Figure 10 respectively, there is a noticeable increase in the density of low-angle grain boundaries and a correspondingly high percentage of high-angle grain boundaries relative to the low-angle boundaries. This higher percentage in high-angle grain boundaries signifies the development of sub-grains during differential speed rolling (DSR) processing, a common

occurrence in continuous dynamic recrystallization (DRX) processes. These newly formed grains are separated by high-angle boundaries.

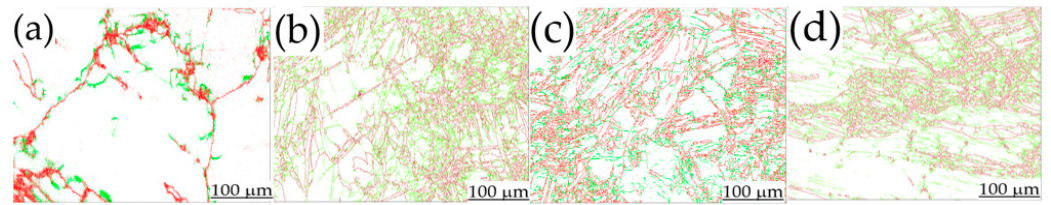


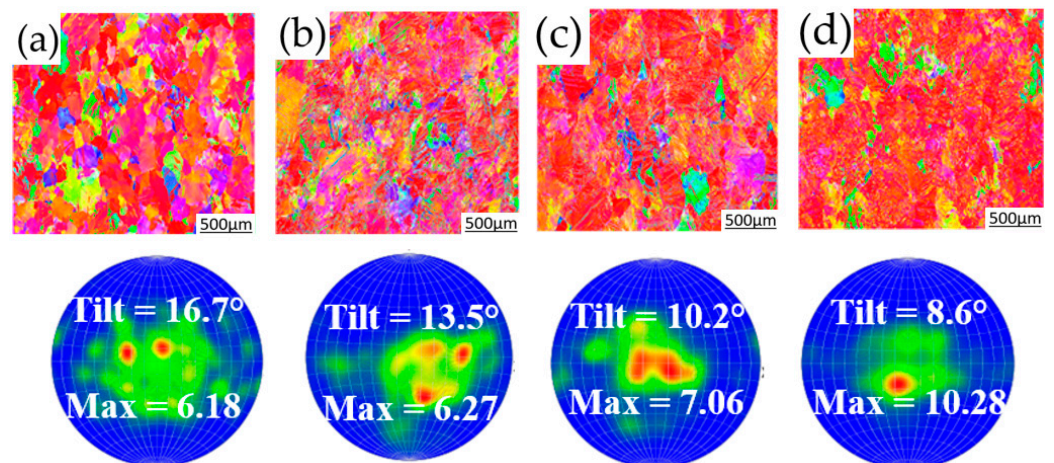
**Figure 10.** Low angle (green) and high angle (red) grain boundaries are highlighted for AXM20504 DSR 4:2 (400 °C) with reductions of (a) 10%, (b) 20%, (c) 30%, and (d) 40%.

However, it is notable that the conversion of low-angle to high-angle grain boundaries was not completed, as indicated in Table 3. This observation suggests that the DRX process was not fully reached, as there wasn't a clear conversion of low-angle to high-angle grain boundaries from 10% to 40% reduction. The incomplete conversion of low-angle boundaries reveals nuances in the microstructural evolution during the rolling process for AXM20504. In addition, the threshold limits of the software posed a limitation in capturing all of the data. For example, the threshold limit for low-angle GB was 2 to 10°, making the capturing of low-angle grain boundaries below 2 degrees not possible. This means the % of low-angle grain boundaries may actually be higher than shown.

**Table 3.** Low Angle and High Angle (%) of AXM20504 at Reductions from 10 to 40%.

Reduction (%)	Low Angle GB (%)	High Angle GB (%)
10	34.6	65.4
20	49.4	50.6
30	41.0	59.0
40	50.9	49.1

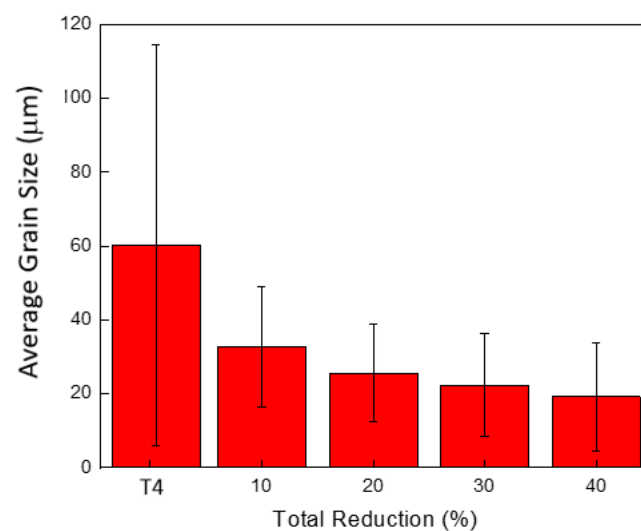
In Figure 11, a comparison of grain refinement is presented for the AXM20504 alloy with successive reductions, along with corresponding pole figures. The grains are larger and coarser in the T4 condition, gradually becoming finer with successive reductions observed at 10%, 20%, 30%, and 40% thickness reductions. This representation highlights the evolution of grain size throughout the rolling process, emphasizing the effectiveness of reduction in achieving grain refinement.



**Figure 11.** IPF maps and corresponding pole figures for AXM20504 from (a) 10%, (b) 20%, (c) 30%, and (d) 40% reduction for DSR at 4:2 m/min rolling speed and 400 °C.

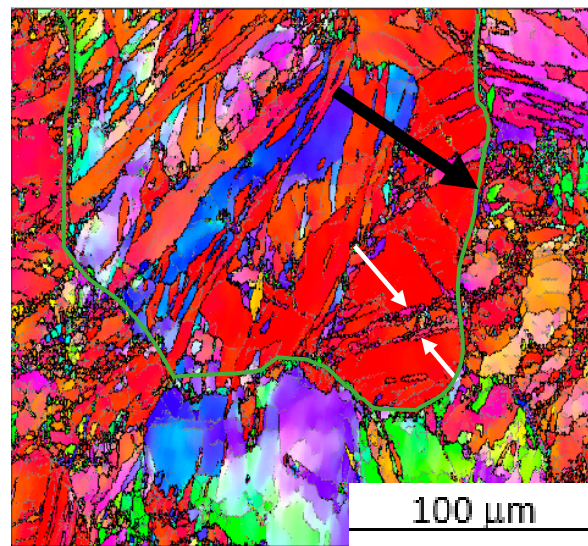
Additionally, the deviation of the pole center (tilt) decreases with increasing thickness reduction, indicating a trend toward a more uniform grain orientation. Simultaneously, the pole intensity increases, signifying a strengthening effect associated with the reduction process. These quantitative measures further contribute to a comprehensive understanding of the microstructural changes induced by successive reductions in the AXM20504 alloy.

Figure 12 displays the average and standard deviation of the grain size, providing quantitative insights into the grain size distribution at different reduction levels. As depicted in Figure 12, the initial T4 average grain size for AXM20504 was  $60.3 \pm 54.3 \mu\text{m}$ . With successive thickness reductions, the grain size decreases to  $31.9 \pm 28.2 \mu\text{m}$  at 10% reduction and further to  $19.5 \pm 14.2 \mu\text{m}$  at 40% reduction. This trend of decreasing grain size with increasing reduction was observed consistently in the other AXM alloys (AXM201504, AXM21004, AXM21504). The quantitative data on grain size provides a clear representation of the impact of the rolling process on refining the microstructure of these alloys. The average grain size includes all grains (i.e., large grains as well as the DRX grains).



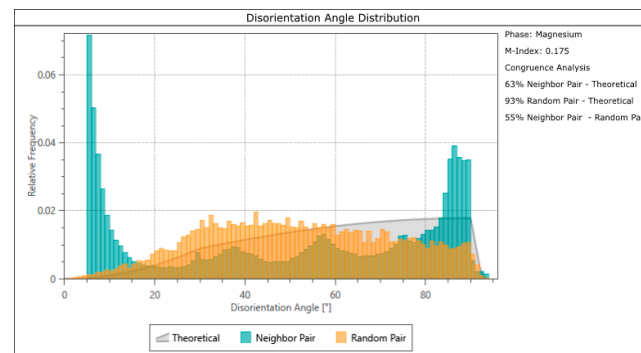
**Figure 12.** Average grain size of AXM20504 alloy for T4 and reductions at 10%, 20%, 30%, and 40% reductions for DSR at 4:2 m/min rolling speed and 400 °C.

Tensile twinning which has the lowest activation energy, refers to the twinning behavior within grains that occurs during hot working, facilitating the DRX process. In this process, high-angle grain boundaries at  $\sim 86^\circ$  are formed by primary or secondary tension twins, and grain boundaries with disorientation angles of  $60^\circ$  are formed by different types of tension twin variants (primary and secondary) [40]. Additionally, nucleation of DRX emerges at the tip of pre-existing twins, and primary and secondary tension twins serve as nucleation sites required for DRX [40]. In some magnesium alloys, such as AZ31, it has been shown that twinning dominates the deformation in DRX with rolling speeds between 3.5 and 12.1 m/min [33]. Furthermore, twinning is more prevalent in magnesium alloys when increasing thickness reduction at similar speeds, resulting in an increase in yield strength but a notable reduction in ductility, as will be demonstrated in the subsequent results. Figure 13 demonstrates twinning-induced DRX and shows the twin bands with DRX along the twin bands throughout the microstructure. Furthermore, the presence of DRX grains in a “necklace-like” arrangement around the deformed grain is seen in Figure 13 as outlined by the green solid line, which is an indication of Discontinuous DRX.

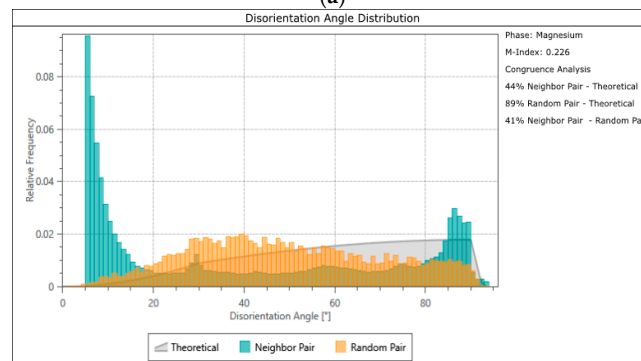


**Figure 13.** IPF Map of AXM20504 at the rolling speed of 4:2 m/min and reduction of 30% DSR at 400 °C demonstrating DRXed grains along twin bands denoted by white arrows. The “necklace-like” arrangement of the DRX grains outlined by the green solid line (black arrows) demonstrates the presence of discontinuous DRX observed.

In Figure 14, the disorientation angle distribution for the AXM20504 obtained from the EBSD analysis is presented, revealing the presence of tensile twinning at an angle of about 86°. The evaluation of the disorientation angle confirms the presence of tensile twinning, a significant aspect of the dynamic recrystallization (DRX) mechanism. Tensile twinning was observed in each successive reduction, with panels (a) through (d) representing 10%, 20%, 30%, and 40%, respectively. Tensile twinning is more prominent at lower reductions, suggesting that it is mostly complete upon reaching higher reductions.



(a)



(b)

**Figure 14.** Cont.

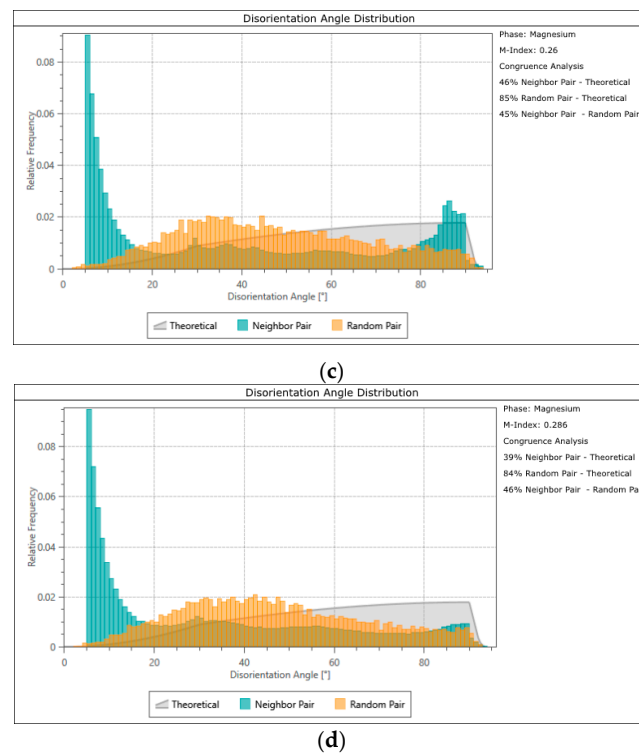


**Figure 14.** Disorientation angle distributions of AXM20504 alloy for reductions (a) 10%, (b) 20%, (c) 30%, and (d) 40% at DSR 4:2 m/min and 400 °C.

### 3.2. Mechanical Properties

The tensile properties of the AXM alloys were systematically evaluated for materials rolled at different rolling speeds and temperature conditions (350, 400, and 450 °C). Figure 15 presents the stress-strain curves for Differential Speed Rolling (DSR) at a 4:2 speed ratio, illustrating the reduction at (a) 10%, (b) 20%, (c) 30%, and (d) 40%. Additionally, a comparison with the T4 state is shown, highlighting a substantial increase in strength for the 40% DSR-rolled material compared to T4, albeit with a noticeable reduction in elongation. This comparison provides a clear indication of the trade-off between strength and ductility, showcasing the impact of the rolling process on the mechanical properties of the AXM alloys. The stress-strain curves offer valuable insights into the material's response to different rolling conditions and the consequent changes in its mechanical behavior.

As depicted in Figure 16, there is a noticeable improvement in yield strength from the T4 to 40% reduction for AXM20504 rolled at all temperatures (Figure 16a). Additionally, there is an enhancement in ultimate tensile strength for all temperatures (Figure 16b). There is an initial increase in elongation, followed by a slight drop after 20% reduction (Figure 16c). Consequently, there is an improvement in the strength of the AXM20504 alloy with a slight compromise in ductility. This trend is consistent across other compositions as well.

It is important to note that these results differ slightly from other studies on differential speed rolled (DSR) magnesium alloys, such as AZ31, where grain refinement led to a significant increase in both strength and ductility, with elongation reaching beyond 18% [33]. Similarly, research on Z5 showed an upward trend in both strength and ductility following DSR [31,32]. The observed drop in ductility after 20% reduction in the AXM alloy is attributed to the strong (0001) basal texture, wherein strength is improved while ductility is slightly decreased based on this preferred orientation and the texture evolution of DRX grains. These variations highlight the alloy-specific behavior and texture development during the rolling process.

The overall trend regarding the influence of strain rate and temperature on the ultimate tensile strength and elongation of all of the AXM alloys is illustrated in Figure 17. In the figure, there is a consistent increase in ultimate tensile strength (UTS) for all AXM alloy compositions at temperatures of 350, 400, and 450 °C. Conversely, there is a slight decrease in percent elongation for all AXM alloys, as observed. This indicates an overall improvement in the strength of the alloys after rolling, with a marginal reduction in elongation (ductility). It's noteworthy that these results differ from observations in other magnesium alloys, where both strength and ductility have been shown to increase through DSR [41]. The unique behavior observed in the AXM alloys underscores the importance of understanding alloy-specific responses to processing parameters. Also, the strain rate used in the work is the effective plastic strain rate that was calculated based on the equation presented by Ko et al. in their paper [42].

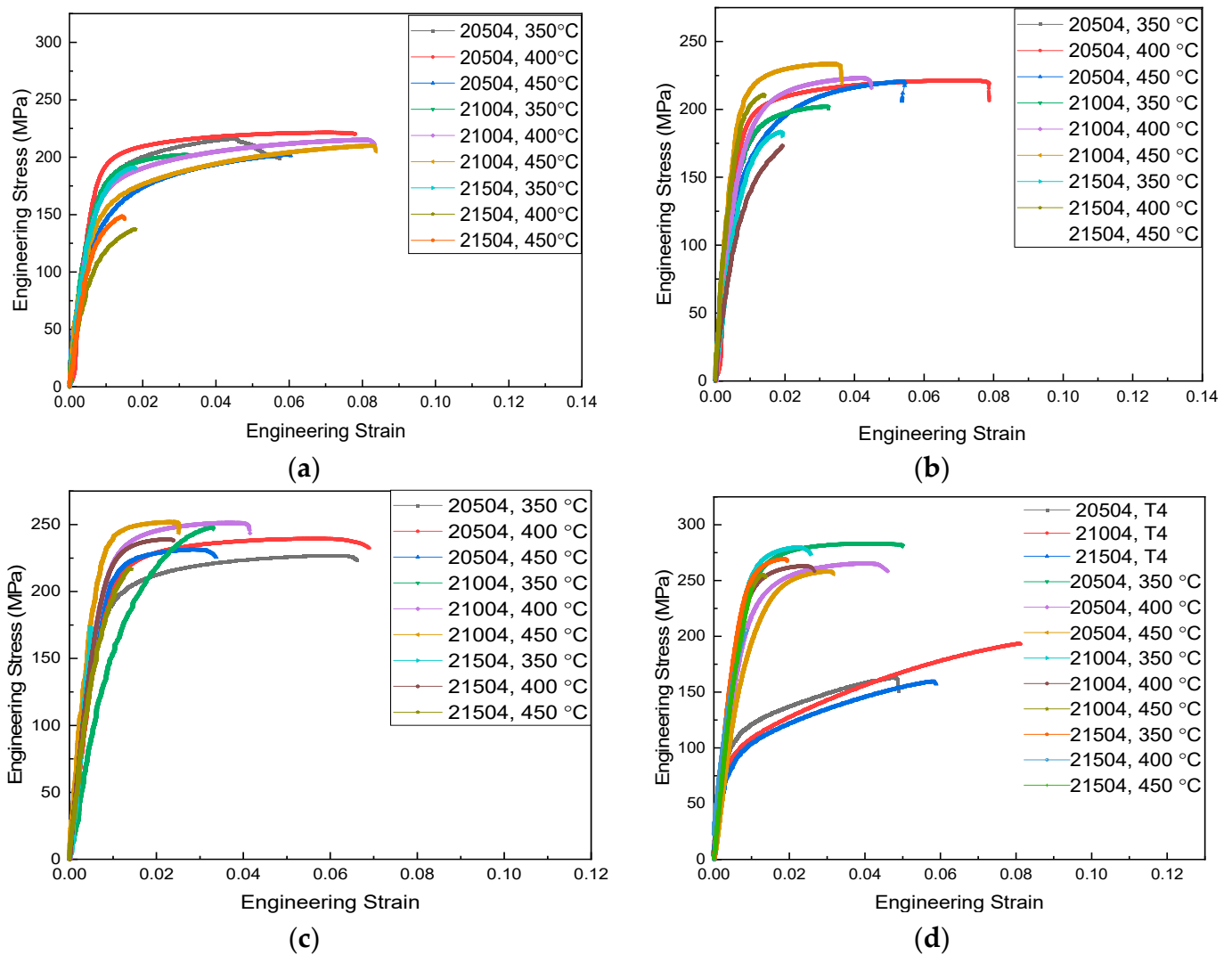


**Figure 15.** Comparison of Stress-Strain curves for AXM alloys at reductions (a) 10% (b) 20%, (c) 30%, and (d) 40% for temperatures 350, 400, and 450 °C using DSR 4:2 speed ratio.

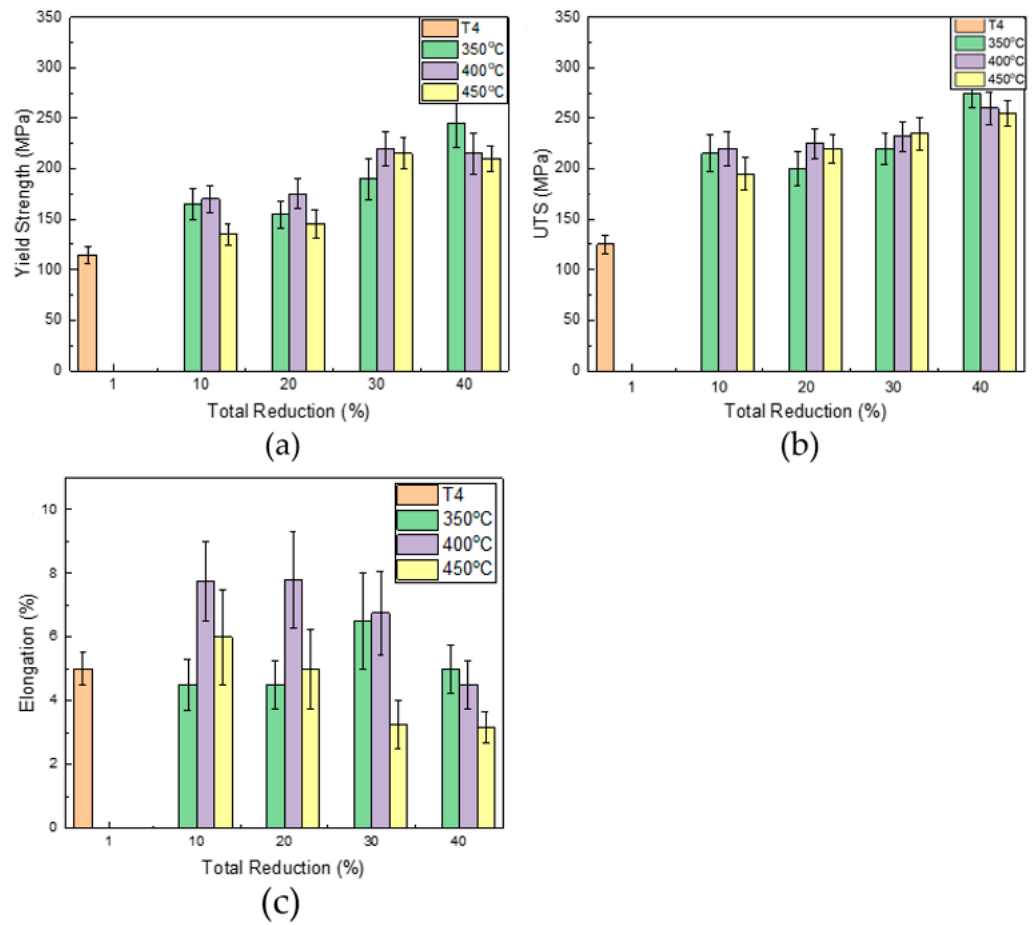


**Figure 16.** Evaluation of (a) Yield Strength, (b) Ultimate Tensile Strength (UTS), and (c) % Elongation for AXM20504 alloys at reductions of 10%, 20%, 30%, and 40% and temperatures 350, 400, and 450 °C processed with DSR 4:2 m/min.

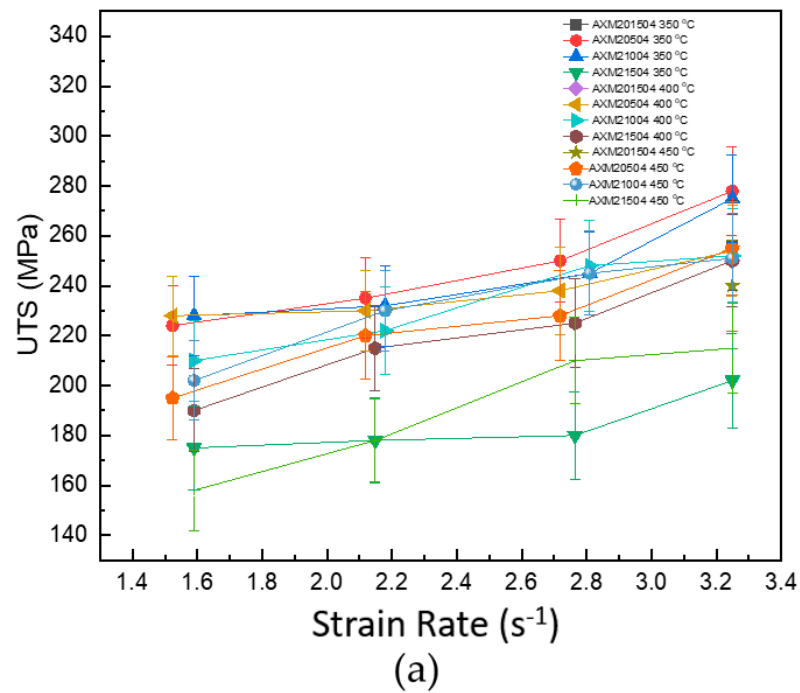


**Figure 17.** Cont.

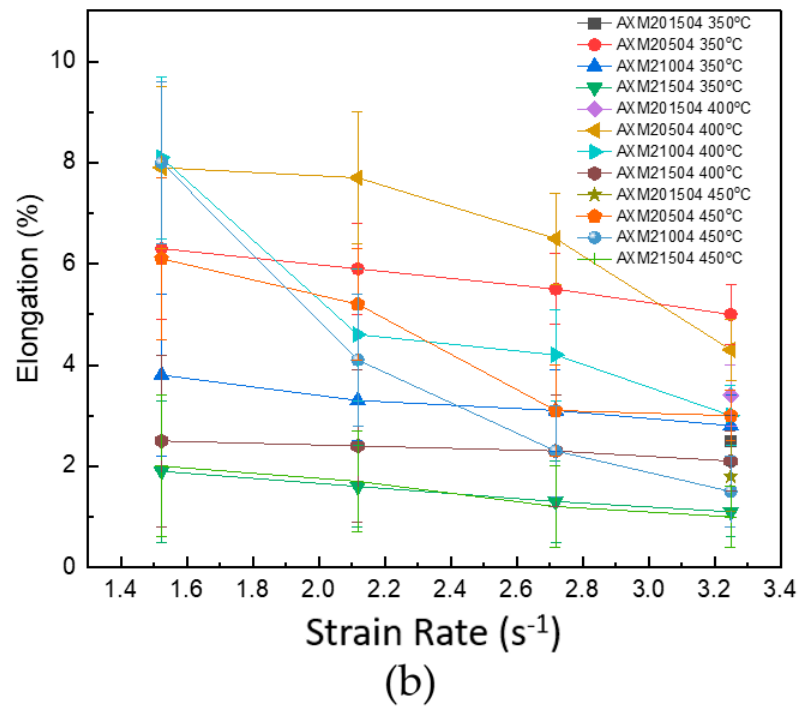


**Figure 17.** Influence of strain rate on (a) UTS and (b) % Elongation for AXM compositions at DSR 4:2 m/min and reductions 10%, 20%, 30%, and 40% with temperatures 350, 400, and 450 °C.

#### 4. Discussion

The microstructural analysis through optical microscopy (OM), scanning electron microscopy (SEM), and electron backscatter diffraction (EBSD), inverse pole figure (IPF) maps revealed an increase in the percentage of dynamically recrystallized (DRXed) grains with successive increases in strain rate, dependent on thickness reduction, rolling speed, and speed difference (speed ratio). Plastic deformation of the material through differential speed rolling (DSR) and conventional rolling (CR) created more fine DRX grains, corresponding to an increase in the strength of the AXM alloys, as observed in the tensile testing from 10 to 40% thickness reduction. In general, the lower pre-heat temperature of 350 °C and intermediate temperature of 400 °C exhibited higher yield strength and ultimate tensile strength and correlated to a more refined grain size.

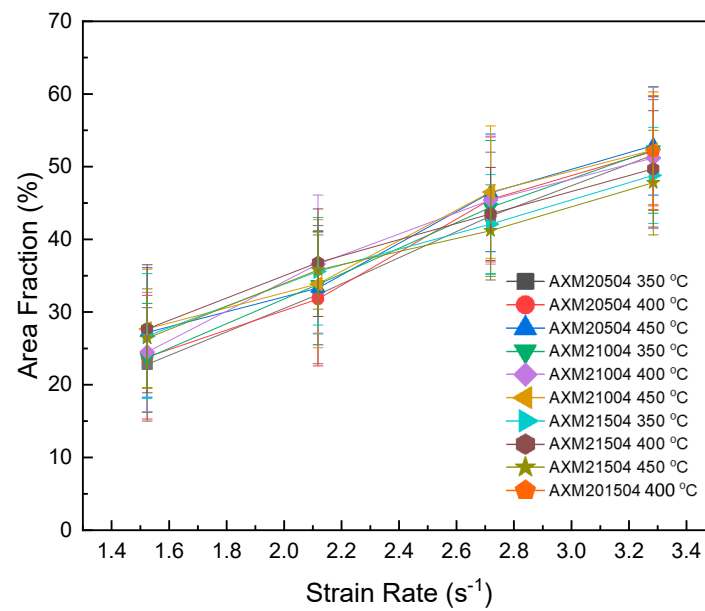
However, at reductions higher than 20%, the elongation (ductility) slightly dropped consistently for all processing temperatures including all alloys. The reduction in ductility is attributed to factors including grain size reduction, being the most important factor in enhancing alloy strength, and a higher basal pole intensity, indicating that grains are more aligned with their basal planes parallel to the surface of the plate (specimen). This alignment leads to higher resistance to deformation, resulting in both higher strength and lower ductility.

Choosing combinations of rolling speeds, thickness reductions, and speed differences for the DSR and CR material was used for analyzing a full range of strain rates and the effect on ultimate tensile strength (UTS) and elongation. The plot of UTS versus strain rate in Figure 17 shows a gradual increase in strength with a corresponding decrease in ductility. It is noteworthy that the strength showed a steady increase, and ductility showed a steady decrease with the increase in strain rate for all AXM compositions. Ductility was higher for alloys with lower Ca compositions, while higher strength occurred for higher Ca compositions.

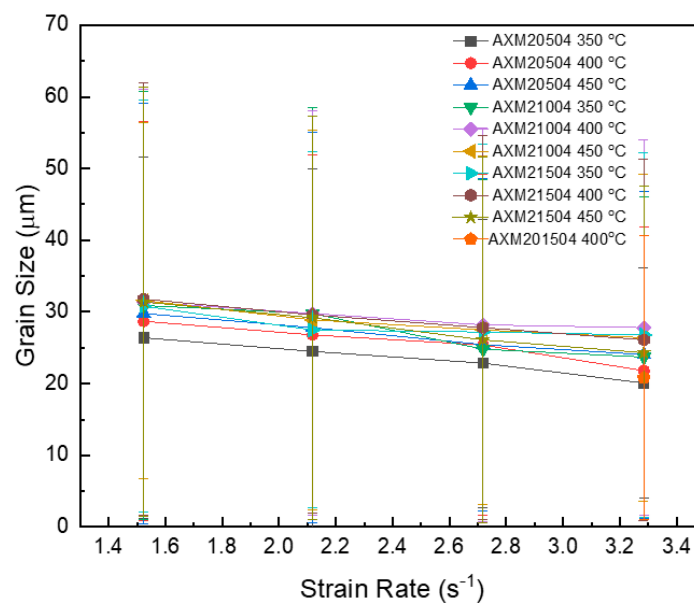
The alloys with the best combination of strength and ductility are those within the mid-range weight percent of Ca. Specifically, AXM20504 and AXM21004 exhibited better combinations of strength and ductility for all temperatures compared to AXM201504 and AXM21504. Furthermore, AXM21504 samples exhibited some appearance of cracking and

brittleness on the edges of the rolled material, especially at 450 °C, likely resulting in lower strength and ductility. The lower Ca weight percent in AXM201504 can explain the lower solution strengthening, leading to lower strength compared to alloys with a higher weight percent of Ca.

Figure 18 illustrates the (a) influence of strain rate on the % Area Fraction of DRX grains, showing a gradual increase with a corresponding increase in strain rate, and (b) the influence of strain rate on average DRX grain size. This increase in grain boundaries and DRX grains correlates with the increase in strength observed in Figure 17. Likewise, there was a gradual decrease in average DRX grain size as seen in Figure 18b. The standard deviation for each of the compositions is relatively consistent and shows the wide range in average grain size as detected in the EBSD software.



(a)



(b)

**Figure 18.** (a) Influence of strain rate on % area fraction of DRX grains in AXM alloys and (b) influence of strain rate on average DRX grain size of AXM alloys for DSR 4:2 m/min at 350, 400, 450 °C.

Various mechanisms were observed in the AXM alloy systems, including twinning DRX, discontinuous DRX, and continuous DRX. Twinning was evident by the DRX grains along twin bands and was observed in all alloy systems at locations of  $86^\circ$  on the disorientation plots for the AXM alloys. Discontinuous DRX was evident in the AXM alloys where the DRX grains formed a ‘necklace’ arrangement, becoming prominent around larger grains during recrystallization. DRX grains were observed around grain boundaries in the AXM alloy systems, where new grain growth occurred along pre-existing grain boundaries. Continuous DRX was observed in the sub-grain evolution of AXM20504 from 10 to 40% reductions, as seen in the low-angle/high-angle grain boundary plots. However, second-phase particles prevalent in the AXM alloys were inferred to retard recrystallization due to the pinning effect of the precipitates on grain boundary migration. It has been demonstrated that fine dynamic precipitates effectively pin grain boundaries to inhibit the growth of DRXed grains, similar to the retarding effect observed in the AXM alloys during the differential speed rolling (DSR) and conventional rolling (CR) hot rolling process [40]. The nucleation and growth of DRX grains can be further understood by considering the Avrami kinetic theory, which accounts for the recrystallized fraction of grains as a function of strain. The initial slow rate is attributed to the time required for a significant number of nuclei of the new phase to form and begin growing. During the intermediate period, the transformation is rapid as nuclei grow into particles and consume the old phase, while nuclei continue to form in the remaining parent phase. Nucleation can occur on specific sites such as grain boundaries or impurities that rapidly saturate soon after the transformation begins. Initially, nucleation may be random and growth unhindered. Once the nucleation sites are all consumed, the formation of new particles will cease [43–49].

The Hall-Petch equation is expressed as  $\sigma_y = \sigma_0 + k/d^{1/2}$ , where  $\sigma_y$  is the yield stress,  $\sigma_0$  is the intercept,  $k$  is the constant, and  $d$  is the grain size [50]. The Hall-Petch effect predicts, in a good approximation, that the smaller the size ( $d$ ) of the grain, the higher the elasticity limit, and  $\Delta\sigma = k/d^{1/2}$ . Figure 19 depicts the fitting of the data for the AXM20504 alloy using the Hall-Petch relationship. It has been observed that a gradual decrease in grain boundary spacing may be followed by an increase in the  $k$  value based on experimental results. Therefore, a plot of the experimental data, where  $\sigma_0$  and  $k$  are considered constants, may be viewed as a relatively rough approximation, not fully capturing the change in grain boundary characteristics as  $d$  decreases with increasing plastic strain. This suggests that the Hall-Petch relationship serves as an approximate model, and the real-world behavior may involve more complex interactions and variations in grain boundary characteristics with plastic strain.

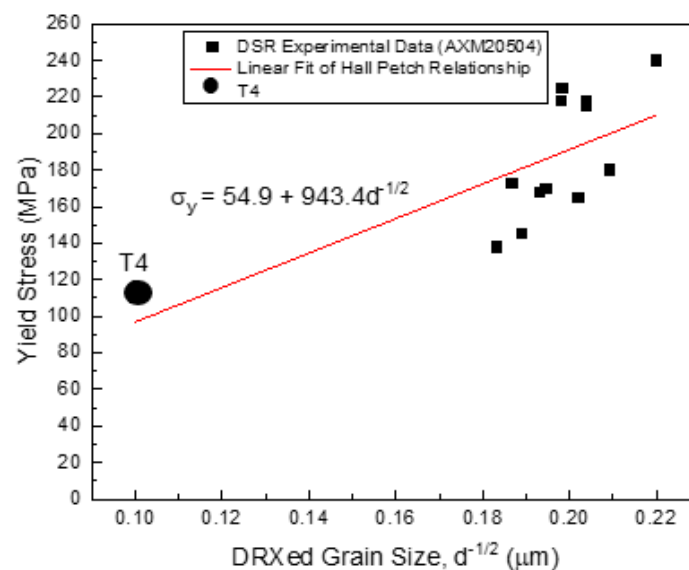


Figure 19. Relationship of AXM20504 DSR data to Hall Petch equation.

The application of the Hall-Petch relation for analyzing the flow stress of deformed materials, such as the AXM alloys, is complex due to the subdivision of the structure by boundaries with different characteristics, showing varying resistances to slip for different systems [51]. For instance, there may be a critical angle for dislocation boundaries below which the boundary resistance increases with an increase in disorientation angle, and above which a dislocation boundary and a high angle boundary show the same resistance, as suggested by Li [51]. The strengthening effect of grain boundaries and deformation-induced high-angle boundaries embedded in a deformation microstructure has not been fully quantified, and further studies with well-characterized structural parameters and high-resolution electron microscopy of boundary structures are needed [52,53].

These studies are crucial not only for analyzing strengthening mechanisms but also for providing guidelines for optimizing structural and mechanical properties by adjusting processing conditions and the response of materials to plastic deformation and alloying [54]. In the AXM alloy systems, which involve moderate strain rates, the extent of DRX increased with increasing strain rate and temperature within the range of hot working parameters. The acceleration of DRX with strain rate is attributed to the increased rate of dislocation accumulation.

## 5. Conclusions

The AXM alloys, containing varying amounts of Ca ranging from 0.15 wt% to 1.5 wt%, were subjected to single-pass differential speed rolling (DSR) and conventional rolling (CR) with different rolling temperatures, thickness reduction rates, as well as different speed ratios. Microstructural characterization techniques, including optical microscopy (OM), scanning electron microscopy (SEM), and electron backscatter diffraction (EBSD), were employed, revealing the occurrence of dynamic recrystallization (DRX). The rolling process resulted in the formation of fine DRX grains, with an increasing area fraction of DRX grains corresponding to incremental increases in strain rate. The average grain size was reduced from  $60.3 \pm 54.3 \mu\text{m}$  (T4) to  $19.5 \pm 14.2 \mu\text{m}$  for DSR 4:2 m/min rolling speed at 40% reduction and 400 °C in single-pass rolling.

The DRX mechanisms observed were twinning DRX, discontinuous DRX, and continuous DRX. The twin bands with DRX grains around them were observed. The twinning commonly observed with 86° disorientation angle for all thickness reductions (strain rates) indicates they are tension twinning. Also, DRX grains were observed in a “necklace-like” arrangement as is characteristic of discontinuous DRX. Continuous DRX was observed in the sub-grain evolution of AXM20504 from 10 to 40% thickness reductions, as seen in the low-angle/high-angle grain boundary plots.

The mechanical properties of the AXM material exhibited a rise in strength with thickness reduction increased to 40% (~strain rate of  $3.3 \text{ s}^{-1}$ ), while ductility increased for the thickness reduction up to 20% for most AXM compositions. The average strength of the materials doubled from  $125 \pm 10.2 \text{ MPa}$  (T4) to  $260 \pm 25.8 \text{ MPa}$ . However, a decrease in ductility of the rolled material was observed with higher thickness reduction. The presence of Ca in AXM20504 and AXM21004 contributed to enhanced strength, whereas alloys with lower (AXM201504) and higher (AXM21504) weight percentages of Ca displayed both a lower strength and ductility. The observed improvement in strength across all compositions was accompanied by a compromise in percent elongation (ductility), a phenomenon commonly observed in magnesium alloy systems. Ongoing studies are underway to evaluate the impact of subsequent annealing on the microstructure, strength, and ductility of AXM alloys, to improve ductility without sacrificing the alloys' strength.

The yield strength and grain size relationship for both DSR- and CR-CR-processed samples were evaluated. It follows a consistent relationship with the Hall-Petch theory. However, more work is needed to analyze the strengthening effect of grain boundaries and deformation-induced high-angle boundaries embedded in a deformation microstructure that needs to be fully quantified. Thus, further studies are needed with well-characterized structural parameters and high-resolution electron microscopy of boundary structures.

**Author Contributions:** Conceptualization, Z.X. and C.H.; methodology, C.H., Z.X. and J.R.; formal analysis, C.H. and Z.X.; investigation, C.H., Z.X., S.F. and J.S.; resources, Z.X., C.H. and J.S.; data curation, C.H. and Z.X.; writing—original draft preparation, C.H. and Z.X.; writing—review and editing, C.H. and Z.X.; visualization, C.H. and Z.X.; supervision, Z.X. and J.S.; project administration, C.H., Z.X. and J.S.; funding acquisition, J.S. and Z.X. All authors have read and agreed to the published version of the manuscript.

**Funding:** Research funding was provided by NSF Manufacturing: CMMI-2026313; Manufacturing of High Strength, High Ductility, Rare Earth-Free Magnesium Alloy Plate and Sheet Materials by Differential Speed Rolling. Also, funding was provided by ERC HAMMER: EEC-2133630; NSF Engineering Research Center for Hybrid Autonomous Manufacturing Moving from Evolution to Revolution.

**Data Availability Statement:** The original contributions presented in the study are included in the article. Further inquiries can be directed to the corresponding author/s.

**Acknowledgments:** All the authors would like to thank the entire team at North Carolina A&T State University who supported this research project.

**Conflicts of Interest:** The authors declare no conflicts of interest.

## References

1. Yan, H.; Xu, S.W.; Chen, R.S.; Kamado, S.; Honma, T.; Han, E.H. Twins, shear bands and recrystallization of a Mg-2.0%Zn-0.8%Gd alloy during rolling. *Scripta Mater.* **2011**, *64*, 141–144. [[CrossRef](#)]
2. Yin, S.; Duan, W.; Liu, W.; Wu, L.; Yu, J.; Zhao, Z.; Liu, M.; Wang, P.; Cui, J.; Zhang, Z. Influence of specific second phases on corrosion behaviors of Mg-Zn-Gd-Zr alloys. *Corros. Sci.* **2019**, *166*, 108419. [[CrossRef](#)]
3. Sameer, M.D.; Birru, A.K. Mechanical and metallurgical properties of friction stir welded dissimilar joints of AZ91 magnesium alloy and AA 6082-T6 aluminium alloy. *J. Magnes. Alloys* **2019**, *7*, 264–271.
4. WChen, Z.; Zhang, W.C.; Zhang, L.X.; Wang, E.D. Property improvements in finegrained Mg-Zn-Zr alloy sheets produced by temperature-step-down multi-pass rolling. *J. Alloys Compd.* **2015**, *646*, 195–203.
5. Nakata, T.; Xu, C.; Ajima, R.; Shimizu, K.; Hanaki, S.; Sasaki, T.; Ma, L.; Hono, K.; Kamado, S. Strong and ductile age-hardening Mg-Al-Ca-Mn alloy that can be extruded as fast as aluminum alloys. *Acta Mater.* **2017**, *130*, 261–270. [[CrossRef](#)]
6. Wang, P.; Guo, E.; Wang, X.; Kang, H.; Chen, Z.; Cao, Z.; Wang, T. The influence of Sc addition on microstructure and tensile mechanical properties of Mg-4.5Sn-5Zn alloys. *J. Magnes. Alloys* **2019**, *7*, 456–465. [[CrossRef](#)]
7. Wei, J.; Chen, J.; Yan, H.; Su, B.; Pan, X. Effects of minor Ca addition on microstructure and mechanical properties of the Mg-4.5Zn-4.5Sn-2Al-based alloy system. *J. Alloys Compd.* **2013**, *548*, 52–59. [[CrossRef](#)]
8. She, J.; Peng, P.; Xiao, L.; Tang, A.; Wang, Y.; Pan, F. Development of high strength and ductility in Mg-2Zn extruded alloy by high content Mn-alloying. *Mater. Sci. Eng. A* **2019**, *765*, 138203. [[CrossRef](#)]
9. Huang, H.; Liu, H.; Wang, C.; Sun, J.; Bai, J.; Xue, F.; Jiang, J.; Ma, A. Potential of multipass ECAP on improving the mechanical properties of a high-calcium-content MgAl-Ca-Mn alloy. *J. Magnes. Alloys* **2019**, *7*, 617–627. [[CrossRef](#)]
10. Li, Z.T.; Qiao, X.G.; Xu, C.; Kamado, S.; Zheng, M.Y.; Luo, A.A. Ultrahigh strength Mg-Al-Ca-Mn extrusion alloys with various aluminum contents. *J. Alloys Compd.* **2019**, *792*, 130–141. [[CrossRef](#)]
11. Wang, H.; Yu, Z.; Zhang, L.; Liu, C.; Zha, M.; Wang, C.; Jiang, Q. Achieving high strength and high ductility in magnesium alloy using hard-plate rolling (HPR) process. *Sci. Rep.* **2015**, *5*, 17100. [[CrossRef](#)] [[PubMed](#)]
12. Bian, M.Z.; Sasaki, T.T.; Suh, B.C.; Nakata, T.; Kamado, S.; Hono, K. A heat-treatable Mg-Al-Ca-Mn-Zn sheet alloy with good room temperature formability. *Scr. Mater.* **2017**, *138*, 151–155. [[CrossRef](#)]
13. Wang, Y.; Kang, S.B.; Cho, J. Microstructure and mechanical properties of Mg-Al-Mn-Ca alloy sheet produced by twin roll casting and sequential warm rolling. *J. Alloys Compd.* **2011**, *509*, 704–711. [[CrossRef](#)]
14. Gong, X.; Li, H.; Kang, S.B.; Cho, J.H.; Li, S. Microstructure and mechanical properties of twin-roll cast Mg-4.5Al-1.0Zn sheets processed by differential speed rolling. *Mater. Des.* **2010**, *31*, 1581–1587. [[CrossRef](#)]
15. Rahmatabadi, D.; Hashemi, R.; Tayyebi, M.; Bayati, A. Investigation of mechanical properties, formability, and anisotropy of dual phase Mg-7Li-1Zn. *Mater. Res. Express* **2019**, *6*, 096543. [[CrossRef](#)]
16. Huang, H.; Tang, Z.; Tian, Y.; Jia, G.; Niu, J.; Zhang, H.; Pei, J.; Yuan, G.; Ding, W. Effects of cyclic extrusion and compression parameters on microstructure and mechanical properties of Mg-1.50Zn-0.25Gd alloy. *Mater. Des.* **2015**, *86*, 788–796. [[CrossRef](#)]
17. Peng, P.; She, J.; Tang, A.; Zhang, J.; Zhou, S.; Xiong, X.; Pan, F. Novel continuous forging extrusion in a one-step extrusion process for bulk ultrafine magnesium alloy. *Mater. Sci. Eng. A* **2019**, *764*, 138144. [[CrossRef](#)]
18. Torbati-Sarraf, S.; Mahmudi, R. Microstructure and mechanical properties of extruded and ECAPed AZ31 Mg alloy, grain refined with Al-Ti-C master alloy. *Mater. Sci. Eng. A* **2010**, *527*, 3515–3520. [[CrossRef](#)]
19. Kang, J.-W.; Sun, X.-F.; Deng, K.-K.; Xu, F.-J.; Zhang, X.; Bai, Y. High strength Mg-9Al serial alloy processed by slow extrusion. *Mater. Sci. Eng. A* **2017**, *697*, 211–216. [[CrossRef](#)]
20. Chen, C.; Chen, J.; Yan, H.; Su, B.; Song, M.; Zhu, S. Dynamic precipitation, microstructure and mechanical properties of Mg-5Zn-1Mn alloy sheets prepared by high strain-rate rolling. *Mater. Des.* **2016**, *100*, 58–66. [[CrossRef](#)]

21. Zubair, M.; Sandlöbes, S.; Wollenweber, M.; Kusche, C.; Hildebrandt, W.; Broeckmann, C.; Korte-Kerzel, S. On the role of Laves phases on the mechanical properties of Mg-Al-Ca alloys. *Mater. Sci. Eng. A* **2019**, *756*, 272–283. [[CrossRef](#)]
22. Kammer, C. *Magnesium-Taschenbuch*; Aluminium-Verlag: Düsseldorf, Germany, 2000.
23. Avedesian, M.M.; Baker, H. *ASM Specialty Handbook: Magnesium and Magnesium Alloys*; ASM International: Almere, The Netherlands, 1999.
24. Lee, Y.C.; Dahle, A.K.; StJohn, D.H. Grain refinement of magnesium. In *Essential Readings in Magnesium Technology*; Mathaudhu, S.N., Luo, A.A., Neelameggham, N.R., Nyberg, E.A., Sillekens, W.H., Eds.; Springer International Publishing: Basel, Switzerland, 2016; pp. 247–254.
25. Zuo, Y.B.; Fu, X.; Mou, D.; Zhu, Q.F.; Li, L.; Cui, J.Z. Study on the role of Ca in the grain refinement of Mg–Ca binary alloys. *Mater. Res. Innov.* **2015**, *19*, S1-94–S1-97. [[CrossRef](#)]
26. Esmaily, M.; Svensson, J.E.; Fajardo, S.; Birbilis, N.; Frankel, G.S.; Virtanen, S.; Arrabal, R.; Thomas, S.; Johansson, L.G. Fundamentals and advances in magnesium alloy corrosion. *Prog. Mater. Sci.* **2017**, *89*, 92–193. [[CrossRef](#)]
27. Cihova, M.; Schäublin, R.; Hauser, L.; Gerstl, S.; Simson, C.; Uggowitzer, P.; Löffler, J. Rational design of a lean magnesium-based alloy with high age-hardening response. *Acta Mater.* **2018**, *158*, 214–229. [[CrossRef](#)]
28. Gneiger, S.; Papenberg, N.P.; Arnoldt, A.R.; Schlögl, C.M.; Fehlbier, M. Investigations of High-Strength Mg-Al-Ca-Mn Alloys with a Broad Range of Ca + Al Contents. *Materials* **2021**, *14*, 5439. [[CrossRef](#)] [[PubMed](#)]
29. Xu, S.; Zhu, C.; Lin, Z.; Jin, C.; Kamado, S.; Oh-Ishi, K.; Qin, Y. Dynamic microstructure evolution and mechanical properties of dilute Mg-Al-Ca-Mn alloy during hot rolling. *J. Mater. Sci. Technol.* **2022**, *129*, 1–14. [[CrossRef](#)]
30. Wang, W.; Chen, W.; Zhang, W.; Cui, G.; Wang, E. Effect of deformation temperature on texture and mechanical properties of ZK60 magnesium alloy sheet rolled by multi-pass lowered-temperature rolling. *Mater. Sci. Eng. A* **2018**, *712*, 608–615. [[CrossRef](#)]
31. Hale, C.; Xu, Z.; Sankar, J. Optimization of Mechanical Properties in Magnesium-Zinc Alloys. In Proceedings of the TMS 2021, Virtual, 15–18 March 2021; pp. 1–16.
32. Xu, Z.; Hale, C.; Zhang, H.; Yarmolenko, S.; Sankar, J. Comparison of Single-Pass Differential Speed Rolling (DSR) and Conventional Rolling (CR) on the Microstructure and Mechanical Properties of Mg<sub>5</sub>Zn. *Bentham Sci.* **2023**, *16*, 431–442. [[CrossRef](#)]
33. Guo, F.; Zhang, D.; Yang, X.; Jiang, L.; Chai, S.; Pan, F. Influence of rolling speed on microstructure and mechanical properties of AZ31 Mg alloy rolled by large strain hot rolling. *Mater. Sci. Eng. A* **2014**, *607*, 1631–1636. [[CrossRef](#)]
34. Sun, H.-F.; Liang, S.-J.; Wang, E.-D. Mechanical properties and texture evolution during hot rolling of AZ31 magnesium alloy. *Trans. Nonferrous Met. Soc. China* **2009**, *19*, s349–s354. [[CrossRef](#)]
35. Lee, J.; Kim, W.; Jeong, H. Microstructure and mechanical properties of Mg-Al-Zn alloy sheets severely deformed by asymmetrical rolling. *Scr. Mater.* **2007**, *56*, 309–312.
36. Li, Z.T.; Zhang, X.D.; Zheng, M.Y.; Qiao, X.G.; Wu, K.; Xu, C.; Kamado, S. Effect of Ca/Al ratio on microstructures and mechanical properties of Mg-Al-Ca-Mn Alloys. *Mater. Sci. Eng. A* **2017**, *682*, 423–432. [[CrossRef](#)]
37. Cao, W.; Chen, S.-L.; Zhang, F.; Wu, K.; Yang, Y.; Chang, Y.; Schmid-Fetzer, R.; Oates, W. PANDAT software with Pan-Engine, PanOptimizer and PanPrecipitation for multi-component phase diagram calculation and materials property simulation. *Calphad* **2009**, *33*, 328–342. [[CrossRef](#)]
38. Zhang, H.; Xu, Z.; Yarmolenko, S.; Kecskes, L.; Sankar, J. Evolution of microstructure and mechanical properties of Mg-6Al alloy processed by differential speed rolling upon post-annealing treatment. *Metals* **2021**, *11*, 926. [[CrossRef](#)]
39. Chang, T.-C.; Wang, J.-Y.; Chia-Ming, O.; Lee, S. Grain refining of magnesium alloy AZ31 by rolling. *J. Mater. Process. Technol.* **2003**, *140*, 588–591. [[CrossRef](#)]
40. Lu, L.; Liu, X.; Shi, D.; Ma, M.; Wang, Z. Effect of Twinning Behavior on Dynamic Recrystallization During Extrusion of AZ31 Mg Alloy. *JOM* **2019**, *71*, 1566–1573. [[CrossRef](#)]
41. Niu, W.; Wang, D.; Wang, G.; Li, J. Recrystallization and Anisotropy of AZ31 Magnesium Alloy by Asynchronous Rolling. *Metals* **2023**, *13*, 1631. [[CrossRef](#)]
42. Ko, Y.G.; Suharto, J.; Lee, J.S.; Park, B.H.; Shin, D.H. Effect of roll speed ratio on deformation characteristics of IF steel subjected to differential speed rolling. *Met. Mater. Int.* **2013**, *19*, 603–609. [[CrossRef](#)]
43. Avramov, I. Kinetics of distribution of infections in networks. *Physica A* **2007**, *379*, 615–620. [[CrossRef](#)]
44. Avrami, M. Kinetics of Phase Change 1. General Theory. *J. Chem. Phys.* **1939**, *7*, 1103–1112. [[CrossRef](#)]
45. Avrami, M. Kinetics of Phase Change 11. Transformation-Time Relations for Random Distribution of Nuclei. *J. Chem. Phys.* **1940**, *8*, 212–224. [[CrossRef](#)]
46. Avrami, M. Kinetics of Phase Change III. Granulation, Phase Change and Microstructure. *J. Chem. Phys.* **1941**, *9*, 177–184. [[CrossRef](#)]
47. Jena, A.K.; Chaturvedi, M.C. *Phase Transformations in Materials*; Prentice Hall: Upper Saddle River, NJ, USA, 1992; pp. 243–247.
48. Cahn, J.W. Transformation Kinetics During Continuous Cooling. *Acta Met.* **1956**, *4*, 572–575. [[CrossRef](#)]
49. Goris, N.A.V.; Castañeda, A.R.S.; Ramirez-Torres, E.E.; Reyes, J.B.; Randez, L.; Cabrales, L.E.B.; Montijano, J.I. Correspondence Between Formulations of Avrami and Gompertz Equations for Untreated Tumor Growth Kinetics. *Rev. Mex. De Fis.* **2020**, *66*, 632–636. [[CrossRef](#)]
50. Callister, W.D. *Fundamentals of Materials Science and Engineering*, 2nd ed.; Wiley & Sons: Hoboken, NJ, USA, 2004; p. 252.
51. Li, J.C.M.; Chou, Y.T. The role of dislocations in the flow stress grain size relationships. *Met. Trans.* **1970**, *1*, 1145–1159. [[CrossRef](#)]
52. Hughes, D.A.; Hansen, N. Deformation structures developing on fine scales. *Philos. Mag.* **2003**, *83*, 3871. [[CrossRef](#)]

53. Wert, J.A. *Microstructural Control in Aluminum Alloys: Deformation, Recovery, and Recrystallization*; Metallurgical Society Inc.: Burlington, ON, Canada, 1986; pp. 67–70.
54. Wang, C.; Kang, J.; Deng, K.; Nie, K.; Liang, W.; Li, W. Microstructure and mechanical properties of Mg-4Zn-xGd (x = 1, 0.5, 1, 2) alloys. *JOM* **2020**, *8*, 451–551. [[CrossRef](#)]

**Disclaimer/Publisher’s Note:** The statements, opinions and data contained in all publications are solely those of the individual author(s) and contributor(s) and not of MDPI and/or the editor(s). MDPI and/or the editor(s) disclaim responsibility for any injury to people or property resulting from any ideas, methods, instructions or products referred to in the content.